Fatigue performance of geosynthetic-reinforced asphalt layers

V. V. Kumar[1], S. Saride[2] and J. G. Zornberg[3]

[1] *Postdoctoral Fellow, Department of Civil, Architectural and Environmental Engineering, University of Texas at Austin, Austin, TX, USA, E-mail: vinay.vasanth@utexas.edu (corresponding author)*
[2] *Professor, Department of Civil Engineering, Indian Institute of Technology Hyderabad, Telangana, India, E-mail: sireesh@ce.iith.ac.in*
[3] *Professor, Department of Civil, Architectural and Environmental Engineering, University of Texas at Austin, Austin, TX, USA, E-mail: zornberg@mail.utexas.edu*

ABSTRACT: This study aims at understanding the influence of different geosynthetic reinforcements on the fatigue performance of asphalt layers and the corresponding mechanisms involved. Three different types of geosynthetic reinforcement, namely a biaxial polypropylene geogrid (PP), a polyester geogrid coated with a polymer-modified binder (PET) and a glass geogrid composite (GGC), were employed to understand the fatigue behaviour of asphalt layers via an asphalt beam fatigue test (ABFT) along with the use of digital image correlation (DIC) techniques. The ABFT results suggest that incorporating geosynthetic reinforcement in the asphalt layers improved the fatigue performance by factors of 11, 27, and 38 for the PP, PET, and GGC specimens, respectively. With the aid of DIC, the mechanisms involved in enhancing the fatigue performance of asphalt layers were effectively evaluated. At failure, a maximum tensile strain of 11.2% was obtained using DIC in control specimens against maximum strain values ranging from 2.7 to 3.8% in geosynthetic-reinforced asphalt specimens. Reductions in layer thickness for the geosynthetic-reinforced asphalt layers on the order of 5.9% (PP), 17.6% (PET), and 23.5% (GGC) were established for the geosynthetics evaluated in this study, based on test results adopted in a design example.

1. INTRODUCTION AND BACKGROUND

In recent years, an exponential increase in roadway traffic volume has resulted in a significantly increased demand on transportation infrastructure. Such increased traffic hinders the effective performance of pavement systems and necessitates frequent maintenance programs (Pasquini *et al.* 2014). The use of geosynthetics has proven effective in substantially enhancing the performance period of existing pavements. Geosynthetics provide functions such as reinforcement, stiffening, drainage, separation, and hydraulic barrier (Khodaii *et al.* 2009; Ferrotti *et al.* 2012; Zornberg 2017a, 2017b). The location of geosynthetics at various levels in the pavement system results in a reduction in rut and permanent deformation (Komatsu *et al.* 1998; Sanders 2001; Correia and Zornberg 2016; Gu *et al.* 2016; Chen *et al.* 2018; Imjai *et al.* 2019; Kazimierowicz-Frankowska 2020),

enhancement of fatigue life (Sanders 2001; Khodaii *et al.* 2009; Virgili *et al.* 2009; Ferrotti *et al.* 2012; Pasquini *et al.* 2014; Gu *et al.* 2016) and alleviation of reflective cracks (Caltabiano 1990; Cleveland *et al.* 2002; Zamora-Barraza *et al.* 2011; Gonzalez-Torre *et al.* 2015; Kumar and Saride 2017; Saride and Kumar 2017; Wargo *et al.* 2017; Sudarsanan *et al.* 2019, 2020). Additionally, the incorporation of geosynthetics within the pavement (mainly asphalt and base) layers may result in a reduction in pavement thickness, thereby minimizing construction costs (Komatsu *et al.* 1998; Correia and Zornberg 2016; Chen *et al.* 2018; Kumar and Saride 2018; Zofka and Maliszewski 2019). However, incorporation of geosynthetics between the asphalt layers has been reported to result in a reduced shearing resistance between asphalt layers, leading to possible delamination between the asphalt layers (Ferrotti *et al.* 2012; Pasquini *et al.* 2014; Kumar and Saride 2017; Saride and Kumar 2017;

Sudarsanan *et al.* 2018). In spite of numerous benefits reported, testing techniques are not well established to clearly identify the mechanisms responsible for the performance improvement of pavement systems with geosynthetic interlayers.

However, recent studies conducted by Safavizadeh *et al.* (2015), Kumar and Saride (2017), Saride and |Kumar (2017, 2019a), Sudarsanan *et al.* (2019), and Wargo *et al.* (2017) have attempted to understand the mechanisms responsible for the performance improvement of geosynthetic-reinforced asphalt overlays regarding minimizing reflection cracking. They combined the dynamic four-point bending tests and Digital Image Correlation (DIC) to assess the growth patterns of reflective cracks and corresponding strains mobilized in the system. The studies reported that DIC was an effective tool to understand the flexural fatigue behavior of geosynthetic reinforced asphalt specimens subjected to repeated loads.

DIC is a non-interferometric optical measurement technique developed in the 1980s to facilitate determination and analysis of the heterogeneities in composites and concrete (Grediac 2004; Romeo 2013). Choi and Shah (1997) and Kim and Wen (2002) successfully adopted the DIC technique to study the deformation characteristics of cement concrete and asphalt concrete specimens, respectively. Further developments in DIC techniques resulted in their successful implementation to assess crack evolution and propagation patterns in the asphalt mixtures. Use of DIC techniques were helpful to advance understanding on the behavior of concrete beams reinforced with high-strength fibers and asphalt beams reinforced with geosynthetics under static and repeated load conditions (Mahal *et al.* 2015; Hamrat *et al.* 2016; Kumar and Saride 2018; Saride and Kumar 2019b). These advances suggest that DIC analysis could be effectively utilized to understand the reinforcement and stress-relieve mechanisms of geosynthetics placed in asphalt layers.

In summary, the incorporation of geosynthetics within asphalt layers have been reported to effectively enhance the performance of asphalt pavements against cracking and permanent deformations. However, the mechanisms responsible for the improvement observed in geosynthetic-reinforced asphalt layers has not been clearly identified. The effectiveness of DIC techniques in providing accurate displacement and strain information on the surface of asphalt layers could potentially provide information on the mechanisms of geosynthetic reinforcement in asphalt layers as well. The present study attempts to identify the various mechanisms of geosynthetics placed in asphalt layers via asphalt beam fatigue tests (ABFT) combined with interpretation of the results using a DIC analysis program. The ABFT and DIC results from this study are incorporated in a pavement design example and evaluated using mechanistic empirical pavement design guidelines (MEPDG) and linear elastic analysis (KENPAVE). Finally, based on the evaluation of the pavement design example, possible reductions in asphalt thickness due to the inclusion of geosynthetics in asphalt layers is proposed.

2. MATERIALS

2.1. Asphalt

An asphalt binder of penetration grade 60/70 was used in the asphalt concrete mix per Ministry of Road Transport and Highways of India (MORTH) specifications (MORTH 2013). Based on an extensive characterization of the asphalt binder properties, it was determined that the binder had a penetration value of 66, a specific gravity of 1.01 and a softening point of 52°C. The flash point and fire points were found to be 340°C and 360°C, respectively. The viscosity of the binder was found to be 460 cP at a temperature of 60°C using a Brookfield viscometer. The particle size distribution of aggregates used in the asphalt concrete mix is presented in Table 1. A Marshall stability test was carried out according to ASTM D6927 to establish an optimum binder content (OBC) for the asphalt concrete mix, and was found to be 5.5% by weight of aggregates. Subsequently, a strength of 14.25 kN and a flow value of 2.5 mm was determined from the Marshall stability test performed on the asphalt concrete mix with an OBC of 5.5%.

2.2. Geosynthetic reinforcements

Three types of geosynthetic materials were selected based on their material composition, aperture size, bonding ability, and working mechanical properties: a biaxial polypropylene (PP) geogrid, a biaxial polyester geogrid coated with a polymer-modified binder coating (PET), and a glass geogrid composite (GGC) (Figure 1).

Manufacturing of the polypropylene geogrid involved extending the polypropylene material along the longitudinal (machine) and lateral (cross-machine) directions. The resulting geogrid had a square aperture of 40 mm. The polyester geogrid was manufactured by knitting together a group of high molecular weight and high tenacity polyester yarns to form a square geogrid with an 18 mm aperture, and by coating them with a polymer-modified binder. The glass geogrid composite consisted of a geogrid composed of glass fibers knitted together and mechanically bonded to a nonwoven geotextile. The tensile and mechanical properties of all the geosynthetic reinforcements were determined by conducting wide-width tensile strength tests according to ASTM D4595. The mean

Table 1. Particle size distribution of aggregates used in the asphalt concrete mix

Sieve size (mm)	Percentage passing (%)
26.5	100
19	85
13.2	68
9.5	60
4.75	43
2.36	35
1.18	26
0.6	20
0.3	14
0.15	9
0.075	4

Polypropylene geogrid (PP)　　　　Polyester geogrid (PET)　　　　Glass geogrid composite (GGC)
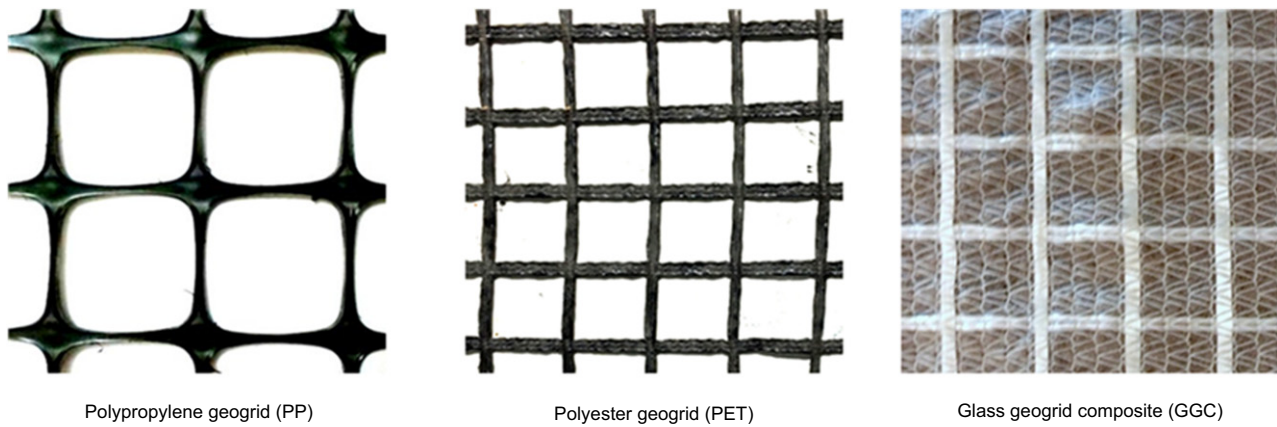
Figure 1. Different types of geosynthetics used in the study

physical and mechanical properties of the geosynthetic reinforcements are presented in Table 2.

2.3. Asphalt specimens

The asphalt concrete mix adopted in the current study was prepared in an asphalt mix plant and transported to the laboratory for specimen preparation. The asphalt mix was stored in the laboratory and the required quantity was heated at 160°C for about 30 min in a hot air oven to facilitate the specimen preparation. Based on the theoretical density and the volume corresponding to the top and bottom layers, the required weight of asphalt mix was calculated separately for each layer. The asphalt layers were then compacted using a 50 N static weight compactor with a square shaped base plate of 200 mm size and using a constant fall height of 500 mm. The number of blows required to compact the asphalt mix was determined separately for each layer and the actual specific gravity of the compacted specimen was determined. An air void content of 6% was maintained in both top and bottom asphalt layers.

The unreinforced and geosynthetic-reinforced asphalt beam specimens used in the asphalt beam fatigue tests and subsequent DIC analysis were prepared in the laboratory in different stages. Initially, an asphalt slab consisting of a 30 mm-thick bottom layer was compacted and allowed to cool to room temperature (Figure 2(a)). Then, a penetration grade 60/70 binder tack was uniformly applied at residual rates of 0.25 kg/m^2 (all specimens except GGC) and 0.75 kg/m^2 (for specimens with GGC) as per MORTH specifications (MORTH 2013). Subsequently, geosynthetic reinforcements were installed (except in unreinforced sections) as shown in Figure 2(b) and a 60 mm-thick top asphalt layer was compacted. Figure 2(c) presents the double-layer asphalt slab with geosynthetic reinforcement at a depth of one-third from the bottom. Subsequently, the asphalt slab was carefully cut into beams measuring 400 mm in length, 50 mm in width and 90 mm in depth (Figure 2(d)), which resulted in an aspect (l/b) ratio of 8. Figure 3 depicts an asphalt beam specimen showing the location of the geosynthetic reinforcement in a four-point load test configuration. In the final stage, the asphalt beams were prepared for DIC analysis by applying a white paint uniformly on the specimen face as shown in Figure 2(e). Black paint was then applied under controlled pressure to produce a random speckle pattern, as shown in Figure 2(f). A detailed procedure to prepare asphalt beam specimens for fatigue tests and DIC analysis is described by Kumar and |Saride (2017, 2018) and Saride and Kumar (2017).

3. TEST METHOD AND MEASUREMENT TECHNIQUES

3.1. Asphalt beam fatigue test

Asphalt Beam Fatigue Tests (ABFT) were conducted on the unreinforced and geosynthetic-reinforced specimens to

Table 2. Properties of geosynthetics adopted in the study

Specifications	Polypropylene geogrid (PP)	Polyester geogrid (PET)	Glass geogrid composite (GGC)
Tensile strength at 2% strain (kN/m)	9.02 (MD)	6.05 (MD)	28 (MD)
	12.22 (CMD)	6.57 (CMD)	– (CMD)
Tensile strength at 5% strain (kN/m)	22.52 (MD)	9.20 (MD)	– (MD)
	24.58 (CMD)	10.07 (CMD)	– (CMD)
Ultimate tensile strength (kN/m)	34.95 (MD)	48.20 (MD)	28 (MD)
	42.00 (CMD)	50.87 (CMD)	25 (CMD)
Strain at ultimate tensile strength (%)	10.82 (MD)	18.8 (MD)	2 (MD)
	12.71 (CMD)	21.33 (CMD)	1.5 (CMD)
Thickness (mm)	4	2	3
Aperture size (mm × mm)	40 × 40	18 × 18	28 × 28

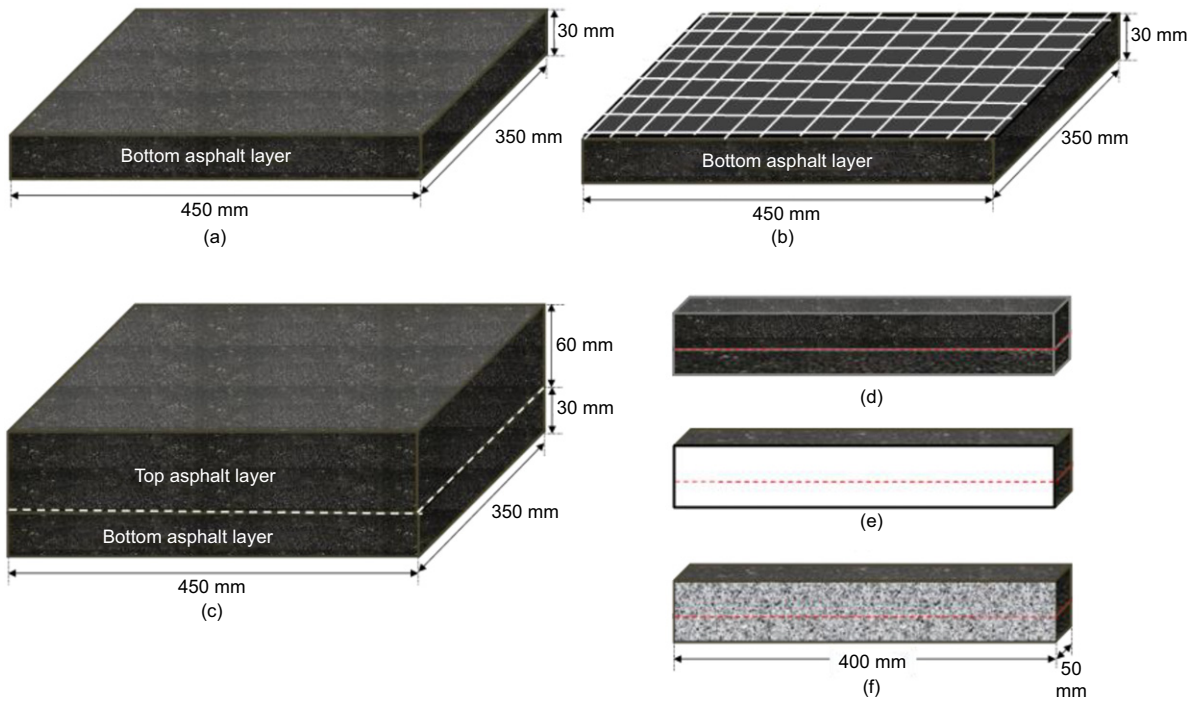*MD: machine direction; CMD: cross-machine direction.

Figure 2. Schematic diagram of specimen preparation procedure adopted for ABFT and DIC analysis in the study: (a) 30-mm thick compacted bottom asphalt layer; (b) installation of tack coat and geosynthetic-reinforcement on bottom layer; (c) two-layered asphalt slab; (d) asphalt beam specimen saw-cut from asphalt slab; (e) application of white paint on asphalt beam specimen face; (f) asphalt beam specimen with random speckle pattern
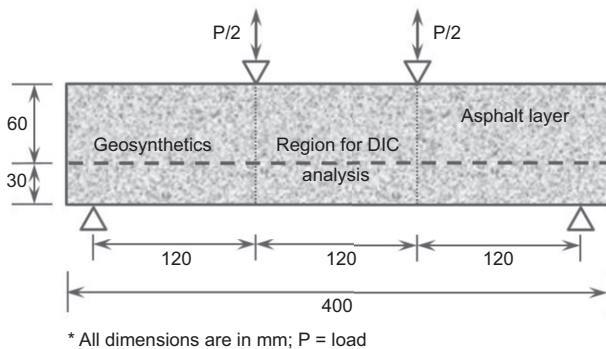

Figure 3. Schematic diagram of asphalt beam specimen and test setup

quantify their fatigue behavior and understand the influence of geosynthetic reinforcements on the performance of asphalt layers. The ABFTs were carried out at a test temperature of $30 \pm 2°C$, under a four-point load configuration, as specified in ASTM D7460. Figure 3 presents a schematic diagram of the asphalt specimen and loading configuration of the test setup used in the study. A fixed distance of 120 mm was maintained between the loading points and roller supports. Additionally, a four-point beam test rig was fabricated to accommodate the asphalt beam specimens, and the load was applied using a servo-hydraulic actuator system. The loads were applied at a frequency of 1 Hz in a typical haversine loading pattern to simulate live traffic conditions. In this regard, a maximum load corresponding to a single axle contact pressure of 550 kPa was found to be 600 N from

back-calculation from:

$$\sigma_f = \frac{Pl}{bh^2} \quad (1)$$

where σ_f is the maximum flexural stress in MPa; P is the maximum load applied in N; and l, b, and h are the span length, width, and thickness of the beam specimen in mm, respectively.

Hence, a maximum load of 600 N and a seating load of 60 N (10% of the maximum load) were applied on the asphalt beam specimens until failure. The corresponding change in vertical deformation was measured at the midpoint of the beam specimen. These vertical deformations could be used to estimate the maximum tensile strains at the end of each load repetition, as follows:

$$\varepsilon = \frac{108\delta \cdot h}{23l^2} \quad (2)$$

where ε is the maximum strain in the specimen; and δ is the vertical deformation in mm at the midpoint of the beam.

However, to understand the geosynthetic reinforcement mechanisms and measure the deformations and corresponding strains mobilized in the specimen, other than that at the bottommost fiber of the specimen, as obtained through Equation (2), DIC was adopted in this study.

3.2. Digital image correlation

The DIC technique was adopted to measure the deformations, curvatures, and strains within specimens by analyzing high-definition images of the specimen surface, which would otherwise be impossible to

measure (e.g. using strain gauges and displacement transducers). DIC is an optical contactless metrology proven successful in estimating the growth of cracks in asphalt layers and concrete beams effectively (Mahal *et al.* 2015; Kumar and Saride 2017). In this study, a 75–300 mm Tamaron lens was mounted to a 5 mega pixel fire wire camera, which was connected to a laptop to record the changes in specimens during the ABFT. The camera and lens assembly were carefully mounted on an adjustable tripod stand with bubble levels, placed approximately 700 mm away from the specimen surface. The height of the tripod was maintained such that the axis of lens was in-line with the specimen surface. Two LED lights were mounted onto separate tripods to provide consistent lighting to the specimen surface. Commercial software, VIC-Snap, was then used to carefully focus and record the continuous images of asphalt beam specimens with a random speckle pattern. A calibration image and an undeformed reference image was recorded prior to initiation of the tests, after which images were recorded at regular time intervals during the ABFT. A two-dimensional digital image analysis program, VIC-2D, was utilized to calibrate the scale and carefully monitor changes in the speckle pattern of the deformed images in relation to the undeformed reference image, and the corresponding full-field displacements and strains were calculated using an iterative technique. The DIC analysis involved choosing the area of interest in the undeformed reference image of the specimen. The deformed images were divided into a number of subsets with the same size, to carefully monitor the changes in gray level (speckle pattern) of each subset with respect to that of the undeformed reference image. The changes monitored in the deformed images were correlated with the undeformed reference image using an iterative Lagrangian approach to compute the full-field displacements and strains. The accuracy of full-field displacements and strains obtained from the DIC analysis depend on the subset size, step size and the filter size adopted for the analysis. Specifically, subset refers to a small area within the area of interest, and the gray level of each subset in the deformed images would be matched with that of the undeformed reference image to compute the displacements. Step size refers to the points analyzed within each subset, and filter size refers to the size of filter adopted to smoothen the strain results. After thorough examination, it was determined that a subset size of 19 pixels, a step size of 1 and a strain filter size of 5 pixels provide accurate

full-field displacements and strains in the specimens tested under ABFT.

4. RESULTS AND DISCUSSION

The ABFTs conducted on unreinforced and geosynthetic-reinforced asphalt beam specimens facilitated understanding the influence of geosynthetic reinforcements on the fatigue behavior of asphalt layers. The results of the ABFTs are summarized in Table 3. As expected, the vertical deformation (VD) increased with increasing load repetitions. For a VD of 1 mm, the fatigue life of all specimens was observed to be comparable, except for the GGC specimens. However, the behavior of the beam specimen changed for increasing VD values, with results that are particularly sensitive to the presence or absence of a geosynthetic reinforcement. The control specimens were found not to resist comparatively high load repetitions failing after 345 load cycles, whereas the specimens with a geosynthetic reinforcement effectively resisted higher load repetitions, ranging from 4000 to 13 500 cycles (i.e. 11 to 38 times higher than the control specimens) prior to failure. This observation indicates that the inclusion of a geosynthetic reinforcement within the asphalt layer enhances the design life of asphalt layers against fatigue cracking. Among the specimens with geosynthetic reinforcements, a fatigue life as high as 13 500 cycles was achieved in GGC specimens, followed by PET specimens at 9500 cycles and PP specimens at 4000 cycles. The different fatigue life values of geosynthetic-reinforced specimens may be attributed to their different mechanical properties.

Furthermore, to investigate the fatigue performance (life) enhancement in geosynthetic-reinforced asphalt specimens against the control specimen, a non-dimensional performance indicator known as fatigue life improvement ratio (I_{NF}) was introduced. The fatigue life improvement ratio was defined as the ratio between the number of load repetitions on a reinforced specimen and the number of load repetitions on a control specimen at the same VD, expressed as follows:

$$I_{NF} = \frac{N_{GR}}{N_{UR}} \tag{3}$$

where N_{GR} and N_{UR} are the number of load cycles corresponding to a reference vertical deformation of

Table 3. ABFT results

Specimen	Number of cycles, N				
	VD = 1 mm	VD = 5 mm	VD = 7.5 mm	VD = 10 mm	Failure
CS	2	115	170	275	345
PP	2	310	1200	2250	4000
PET	5	690	2300	4400	9500
GGC	20	3350	8500	10500	13500

*VD: vertical deformation.

geosynthetic-reinforced and unreinforced specimens, respectively.

The fatigue life improvement factors of geosynthetic-reinforced specimens for increasing reference vertical deformation values are presented in Figure 4. The results indicate a clearly increasing trend in the I_{NF} with increasing reference VD values. For a VD of 1 mm, the I_{NF} values amongst the geosynthetic-reinforced specimens were comparable. However, the I_{NF} of GGC specimens is consi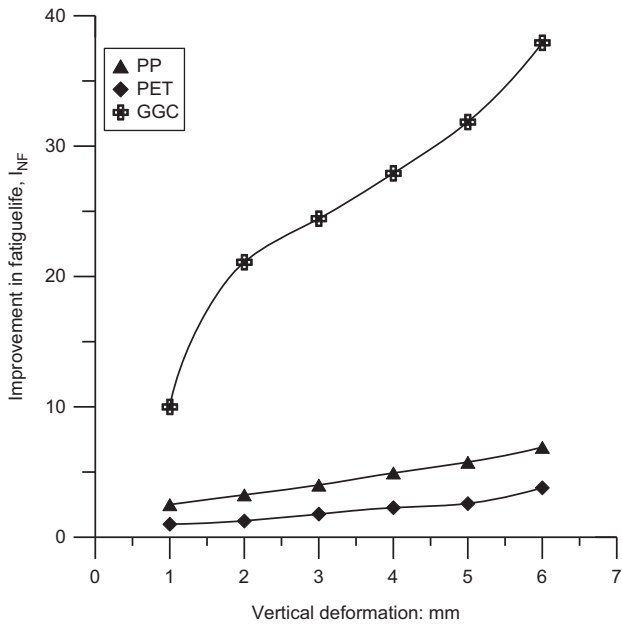stently higher than those for the PP and PET geogrids. This may be attributed to its ability to mobilize its ultimate tensile strength at a comparatively low strain (2%). The PET specimens' I_{NF} were also consistently higher than those for the PP specimens, even though the PP geogrids have a higher initial stiffness than the PET geogrids. The comparatively inferior performance of the PP geogrids could be attributed to their higher initial stiffness, resulting in a reduction of interface bonding between the asphalt layers. Overall, at a VD of 6 mm, I_{NF} values of 38, 7, and 4 were obtained for the GGC, PET, and PP specimens, respectively.

The various geosynthetic reinforcement mechanisms contributing to the enhancement of the fatigue performance of the asphalt layers were subsequently investigated with the aid of DIC analysis. The high-definition images recorded during testing were analyzed and the deformation fields were obtained at the end of the various load cycles. The deformation fields along the beam depth are presented as color-coded deformation bands in Figure 5. A negative deformation value represents a downward movement of the beam and the vertical deformations being the same at the boundary of different color bands. The maximum curvature of the beam specimens can be observed at their midpoint, as is evident from Figure 5. Furthermore, the deformation bands displayed for the control specimen are continuous, while those for the geosynthetic-reinforced specimens are irregular and discontinuous. This can be attributed to the presence of geosynthetics (PP, PET, and GGC) within the asphalt layers, which effectively restricted vertical crack growth and deformations. It is also notable that all specimens failed at nearly the same VD (12.8–13.7 mm), but the number of load repetitions sustained in each case varied. For instance, the control specimen resisted only 345 load
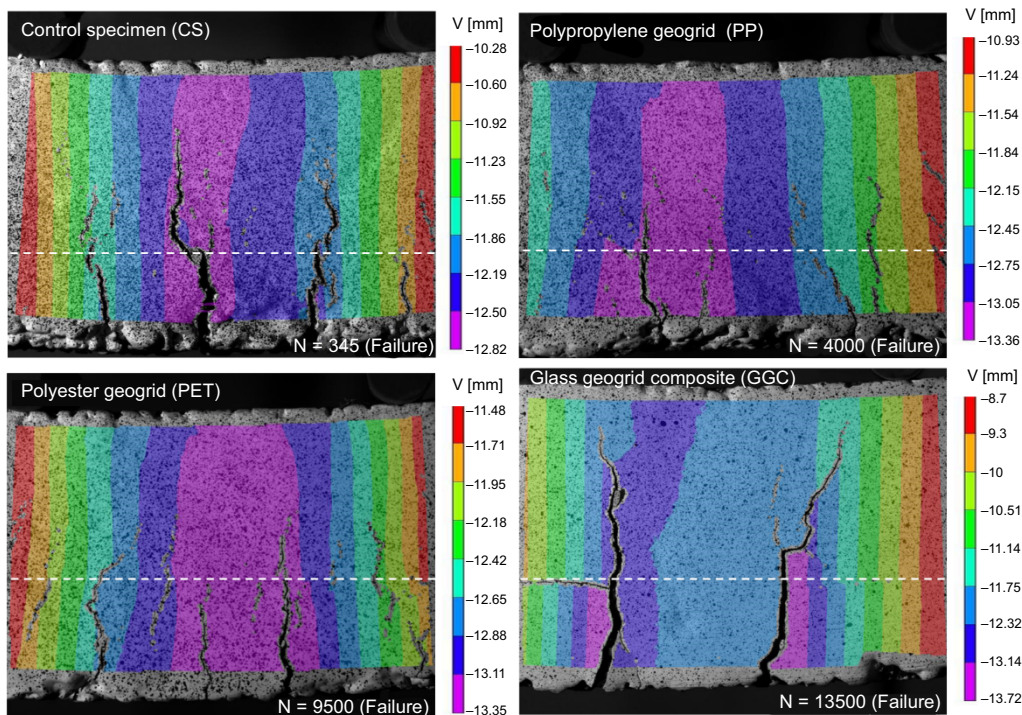

Figure 4. Variation of improvement in fatigue life with vertical deformation

Figure 5. Vertical deformation bands at failure

repetitions before failure, whereas geosynthetic-reinforced beams resisted load repetitions of 4000 (PP), 9500 (PET), and 13 500 cycles (GGC). These results suggest that the geosynthetics predominantly restricted vertical crack growth and retarded the rate of reduction in beam stiffness by carrying the tensile stresses that are ultimately responsible for crack growth in the asphalt layers.

The tensile strain contours corresponding to crack initiation and failure for all specimens are shown in Figure 6. As can be observed, cracking initiated at 20, 60, 80, and 100 load repetitions in the control, PP, PET, and GGC specimens, respectively. The differences in the number of cycles needed to trigger cracking could be attributed to the reinforcing mechanism of the geosynthetic reinforcements placed between the asphalt layers, which can be detected comparatively early (e.g. for a VD of 1 mm, see Table 3). The tensile strains corresponding to crack initiation ranged from 0.75% to 1% for all specimens. Subsequently, the tensile strain drastically

increased to values as high as 11.2% in the control specimens, causing complete fracture after 345 load cycles. In contrast, tensile strains in the geosynthetic-reinforced specimens ranged from 1.2% to 2.1% at the same number (345) of load cycles, which is roughly 80% to 90% lower as compared to the control specimens.

Depending on their tensile properties, geosynthetics can induce a reinforcing mechanism that carries the tensile stresses responsible for crack growth, thereby restricting vertical crack growth. The GGC specimens were able to effectively arrest the crack growth rate up to 13 500 load repetitions. The maximum tensile strain in the GGC specimens at failure was about 3.1%, corresponding to a 72% reduction with respect to the control specimens. Similarly, the PP and PET specimens reached a 66% and 75% reduction in tensile strains at the end of 4000, and 9500 load cycles, respectively, before failure. These variations amongst the performances of geosynthetic-reinforced specimens may be attributed to their ability to
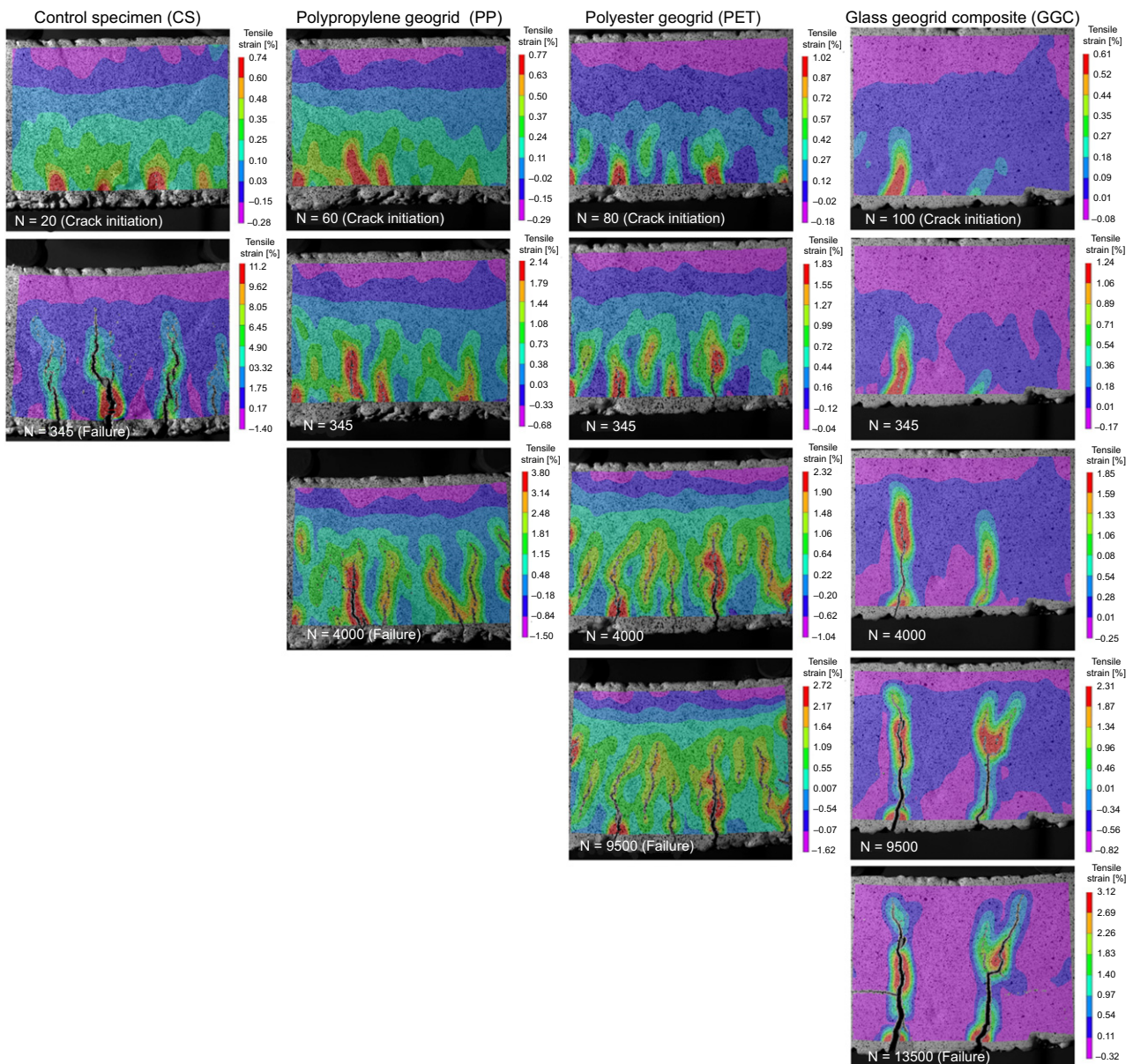

Figure 6. Tensile strain contours

develop reinforcing mechanisms within the asphalt layers. These observations agree with the ABFT results, presented in Table 3 and Figure 4.

Equation (2) predicts the maximum tensile strain at the bottommost layer in the beam specimens. However, the maximum tensile strain is mobilized at the crack tip, which is difficult to obtain using bending theory. Figure 7 presents a comparison of tensile strains calculated using the bending equation and those obtained from digital analysis for all the specimens. The tensile strain trends, as a function of number of cycles, for both cases are in good agreement. However, for the control specimen, a high tensile strain of 11.2% had accumulated at the crack tip at failure, as captured by DIC analysis, as compared to a 4% tensile strain calculated using Equation (2), indicating a higher level of accuracy obtained through DIC analysis over conventional theoretical calculations.

Another important finding obtained from the DIC analysis was that the tensile strain increased to a maximum value when the crack reached the geosynthetic reinforcement (interface zone) and then dropped suddenly. This phenomenon could be due to the presence of the geosynthetic reinforcements, which would absorb the crack energy. The cracks subsequently propagated along the interface zone. The load cycles corresponding to the decrease in tensile strain from the peak value suggest the possibility of delamination between the asphalt layers in the geosynthetic-reinforced asphalt beam specimens.

The inclusion of geosynthetic reinforcements between the asphalt layers has proven effective in restricting vertical crack growth by redirecting cracks in the horizontal direction. The redirection of the crack path often led to an increase in the vertical strains at the interface zone, possibly resulting in the delamination of asphalt layers, as depicted in Figure 8. A pronounced maximum vertical strain of 1.82% was observed for GGC specimens, while vertical strains of 1.28% and 0.93% were recorded for PP and PET specimens, respectively. These values denote a very high intensity of delamination in the GGC specimens due to the absence of apertures. The PP and PET geogrids have 40 mm and 18 mm aperture sizes, respectively, to facilitate through-hole bonding between the asphalt layers. It should also be noted that the PP geogrid, with its larger aperture size (40 mm), is prone to a higher rate of delamination as compared to that of the PET geogrid, with its smaller aperture size (18 mm). This is due to the high initial flexural rigidity, smooth surface characteristics and thickness of a PP geogrid. In contrast, the superior bonding observed for PET geogrids could be attributed to its apertures, which interlock the asphalt concrete mix and polymer-modified binder coating on the geogrids, thus enhancing the bonding ability with the asphalt layers. These trends highlight that, along with the tensile properties of a geosynthetic, it is also important to consider bonding ability with the asphalt layers when adopting a geosynthetic as an asphalt reinforcement.
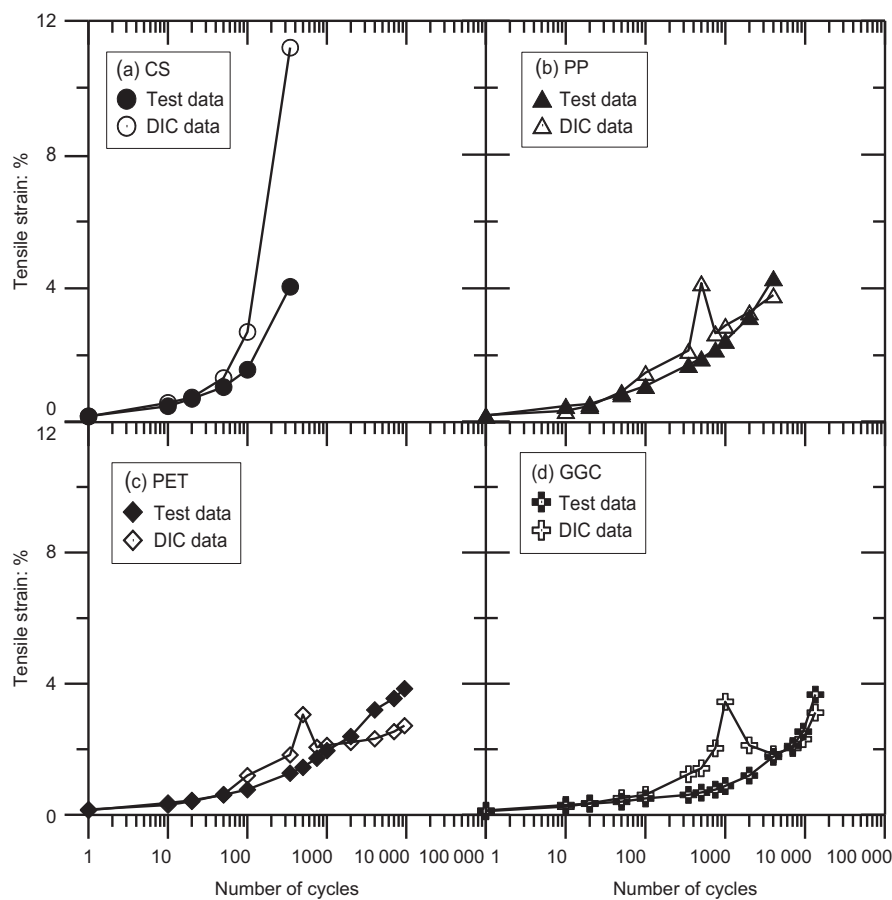

Figure 7. **Comparison of tensile strains: (a) control specimen (CS); (b) polypropylene geogrid (PP); (c) polyester geogrid (PET); (d) glass geogrid composite (GGC)**
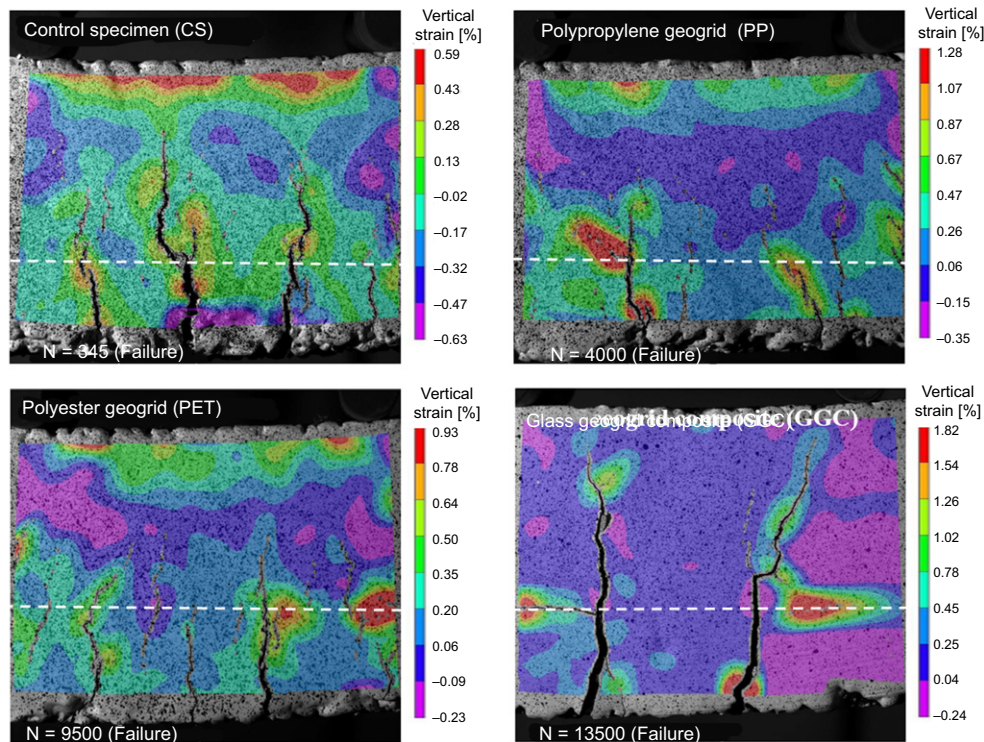
Figure 8. Vertical strain contours at failure

Typical asphalt beam specimens at failure are presented in Figure 9, which show that no lateral creep or deformation can be observed due to the presence of geosynthetics in the asphalt beam specimens tested in this study.

Table 4 presents a summary of crack growth characteristics as measured in crack width (CW) and crack height (CH). The mean crack opening (CW) and crack growth in the vertical direction (CH) were estimated with the help of

(a)

(b)

Figure 9. Typical asphalt beam specimens at failure: (a) control specimen (CS); (b) polypropylene geogrid (PP)

inbuilt tools, such as Crack-Opening Displacement (COD) and point tools, respectively. It can be observed that at an initial VD of 2 mm, the crack growth in terms of CW and CH was prominent in the control specimens, whereas the geosynthetic-reinforced specimens resisted the crack initiation process via a reinforcing effect. Thereafter, the vertical deformation increased with an increase in the number of load cycles, and the CW and CH were observed to eventually increase. However, a significant finding is that the specimens with geosynthetic reinforcements resisted crack initiation and as a result arrested the rate of crack growth substantially. For example, at a VD of 2 mm, there is no indication of crack growth in specimens with geosynthetic reinforcements, while the control specimens exhibit a CW and CH of 0.03 mm and 8.3 mm, respectively. Similarly, the CW and CH at a VD of 5 mm in specimens with geosynthetic reinforcements was determined to range from 0.08 to 0.13 mm and from 33 to 43 mm, respectively, as compared to a CW and CH of 0.15 mm and 55.5 mm, respectively, in control specimens. Nonetheless, a number of micro-cracks did develop at high vertical deformation ranges, especially in PP and PET geogrid-reinforced asphalt beams.

At 345 cycles, prior to failure, a maximum crack opening of 0.6 mm and vertical crack length of 76 mm was observed in control specimens, whereas a crack opening of roughly 0.04 mm to 0.13 mm and crack length of roughly 26 mm to 34 mm (interface zone) was observed in the geosynthetic-reinforced specimens, respectively. At the end of 4000, 9500, and 13 500 cycles, before failure, a maximum crack opening of 0.54 mm, 0.51 mm, and 0.58 mm, and a maximum crack length of 55 mm, 53 mm, and 70 mm were
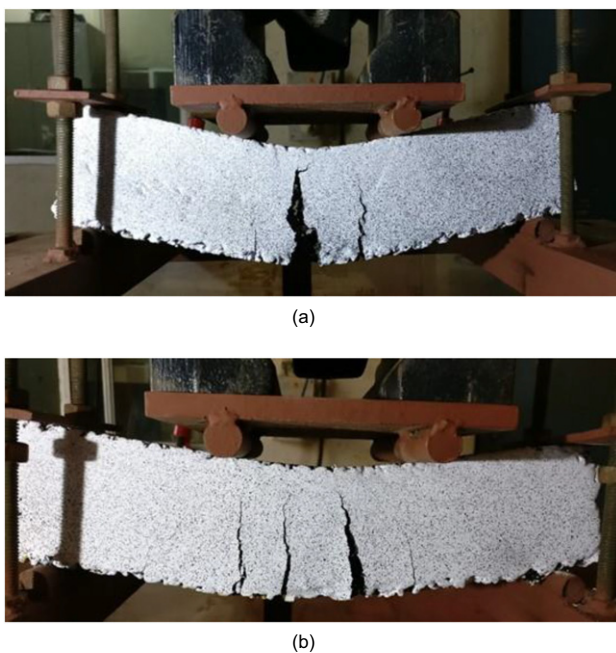
Table 4. Summary of crack growth: DIC analysis

Specimen	VD = 2 mm		VD = 5 mm		VD = 7.5 mm		VD = 10 mm		Failure	
	CW (mm)	CH (mm)	CW (mm)	CH (mm)	CW (mm)	CH (mm)	CW (mm)	CH (mm)	CW (mm)	CH (mm)
CS	0.03	8.3	0.14	47.5	0.28	55.5	0.48	67.5	0.61	75.7
PP	—	—	0.12	33.8	0.18	44.91	0.42	47.9	0.54	54.6
PET	—	—	0.08	33.5	0.18	44.3	0.33	47.5	0.51	52.9
GGC	—	—	0.13	42.9	0.24	49.2	0.45	63.4	0.56	68

*VD: vertical deformation; CW: crack width; CH: crack height.

observed in PP, PET, and GGC specimens, respectively. However, to evaluate the performance improvement in geosynthetic-reinforced specimens, the Normalized Complex Modulus (NCM) values of reinforced specimens were compared with those of control specimen at 345 cycles, using Equation (4).

$$\text{NCM} = \frac{S_i \times N_i}{S_0 \times N_0} \tag{4}$$

where NCM is the normalized complex modulus; S_i is the stiffness of the asphalt beam at ith cycle in MPa; N_i is ith cycle; S_0 is the initial stiffness of the asphalt beam in MPa; and N_0 is the cycle corresponding to the initial stiffness (i.e. after the first load cycle).

The NCM values for the control and the geosynthetic-reinforced specimens were calculated at 345 cycles (corresponding to failure of the control specimen). Also, modulus improvement factors (MIF), defined as a ratio of NCM of reinforced asphalt layer to the NCM of unreinforced asphalt layer, for geosynthetic-reinforced specimens were estimated as 1.45, 2.11, and 2.77 for PP, PET, and GGC specimens, respectively. This improvement in modulus of geosynthetic-reinforced asphalt layers often result in an enhanced service life or a possible reduction in the asphalt layer thickness, in turn reducing construction and maintenance costs. Hence, a typical flexible pavement design example has been considered to demonstrate the possible reduction in the asphalt layer thickness, based on the MIFs determined from the current study for geosynthetic-reinforced asphalt specimens. Performance of the system considered in the design example (conventional pavement layer thickness and reduced asphalt layer thickness for the geosynthetic-reinforced case) was verified, based on the Mechanistic-Empirical Pavement Design approach proposed by the American Association of State Highway and Transportation Officials (AASHTO 1993). In addition, the fatigue strains and rutting strains were calculated using a linear elastic analysis (KENPAVE 2003) and verified with the limiting fatigue and rutting strain equations provided by the Asphalt Institute (1981) for the fatigue and rutting design life.

5. DESIGN EXAMPLE

A typical three-layer flexible pavement section is considered, which involves a design traffic volume of 20 Million Standard Axles (MSA). The thickness and elastic modulus of asphalt concrete layer and granular layers are 216 mm and 2100 MPa; and 483 mm and 200 MPa, respectively. The elastic modulus of subgrade soil was considered as 75 MPa.

5.1. Mechanistic-empirical pavement design guidelines for pavement structures (AASHTO)

The AASHTO design approach is based on the concept of Structural Number (SN) and suggests that SN_actual should be greater than $\text{SN}_\text{reqd.}$ for an adopted pavement layer thickness to safely withstand the design traffic volume without any failure. The $\text{SN}_\text{reqd.}$ and SN_actual for design traffic and pavement layer properties were calculated using Equations (5) & (6) respectively, as per AASHTO guidelines for Design of Pavement Structures (AASHTO 1993).

$$\begin{aligned} \log_{10}(W_{18}) &= Z_\text{R} S + 9.36 \log_{10}(\text{SN} + 1) - 0.2 \\ &+ \frac{\log_{10}[\Delta\text{PSI}/(4.2 - 1.5)]}{0.40 + (1094/(\text{SN} + 1)^{5.19})} \\ &+ 2.32 \log_{10}(M_\text{R}) - 8.07 \end{aligned} \tag{5}$$

where W_{18} is the total 18-kip traffic in equivalent single axle load (ESAL); $Z_\text{R} = -1.282$ is the standard normal variate corresponding to 90% reliability; $S = 0.49$ is the overall standard deviation for flexible pavements; $\text{SN} = \text{SN}_\text{reqd.}$ is the minimum structural number required for a safe pavement design; ΔPSI is the overall serviceability index $= P_0$ (initial serviceability index: 4.2) $- P_t$ (terminal serviceability index: 2); and M_R is the resilient modulus of subgrade in MPa.

$$\text{SN} = (a_1 d_1) + (a_2 d_2 m_2) \tag{6}$$

where $\text{SN} = \text{SN}_\text{actual}$ is the actual structural number of the pavement section considered in the study; a_1 and a_2 are surface and base layer coefficients, presented in Equations (7) & (8), respectively; d_1 and d_2 are thickness of surface and base layers in mm, respectively; m_2 is the drainage coefficient of base layer.

$$a_1 = 0.171 \log_n(M_\text{R-AC}) - 1.784 \tag{7}$$

$$a_2 = 0.249 \log_n(M_\text{R-Base}) - 0.977 \tag{8}$$

where a_1 and a_2 are surface and base layer coefficients, respectively; $M_\text{R-AC}$ and $M_\text{R-Base}$ are resilient modulus of asphalt layer and base layer, respectively in MPa.

The minimum $SN_{reqd.}$ and SN_{actual} for the unreinforced pavement section were determined to be 4.592 and 5.738, respectively, using Equations (5) & (6), respectively. These values indicate that the adopted pavement layer thickness can safely withstand a design traffic of 20 MSA. However, inclusion of geosynthetic reinforcements in the asphalt layer resulted in modulus improvement for the asphalt layer of 1.45 (PP), 2.11 (PET), and 2.77 (GGC) times that of the control specimen for the geosynthetic products evaluated in this study. Subsequently, an increase in SN_{actual} was obtained for pavement sections with geosynthetic-reinforced asphalt layers in the order of 6.278, 6.823, and 7.218 for PP, PET, and GGC specimens, respectively. The increased SN_{actual} values suggest a possible reduction in asphalt layer thickness, without compromising the performance of the pavement section and eventually a reduction in asphalt layer thickness by 12.5 mm (5.9%) for PP reinforced, 38 mm (17.6%) for PET reinforced, and 50 mm (23.5%) for GGC reinforced asphalt layers were proposed. The SN_{actual} for reduced asphalt layer thickness was determined as 6.058, 6.069, and 6.120 for PP, PET, and GGC specimens respectively, which is greater than SN_{reqd}.

5.2. Linear elastic analysis (KENPAVE)

Linear elastic analysis of the design flexible pavement section was performed using KENPAVE (2003) and involved determining the horizontal tensile (fatigue) and vertical compressive (rutting) strains below the asphalt layer and on top of subgrade, respectively, for a design traffic of 20 MSA. It is expected that the strains obtained from KENPAVE analysis would be less than the limiting fatigue and rutting strains, for an adopted pavement layer thickness to safely withstand the design traffic without any failures. The limiting fatigue and rutting strains for the design traffic were calculated using

Equations (9) & (10), respectively, as per Asphalt Institute guidelines for Thickness Design – Asphalt Pavements for Highways and Streets (Asphalt Institute, 1981).

$$N_f = 0.00432C\left(\frac{1}{\varepsilon_t}\right)^{3.291}\left(\frac{1}{M_{R-AC}}\right)^{0.854} \tag{9}$$

$$N_R = 1.365 \times 10^{-9}\left(\frac{1}{\varepsilon_v}\right)^{4.477} \tag{10}$$

where N_f and N_R are the fatigue and rutting life of a flexible pavement system; ε_t and ε_v are the limiting fatigue and rutting strains for design fatigue/rutting life; M_{R-AC} is the resilient modulus of asphalt layer; and $C = 10^M$ is an adjustment factor for the variation in volumetric parameters of the asphalt mix.

$$M = 4.84\left(\frac{V_b}{V_a + V_b} - 0.69\right) \tag{11}$$

where V_a is the percentage air voids in the asphalt mix used in the bottom asphalt layer; and V_b is the percentage effective volume of bitumen in the asphalt mix used in the bottom asphalt layer.

The input values used in the KENPAVE analysis to determine the fatigue and rutting strains for conventional pavement layers (unreinforced pavement section) and geosynthetic-reinforced pavement layers with reduced asphalt layer thickness (geosynthetic-reinforced pavement section) are provided in Table 5.

The limiting fatigue and rutting strains obtained from Equations (9) & (10), for a design traffic of 20 MSA were in the order of 7.6×10^{-4} and 2.45×10^{-4}, respectively and the results from KENPAVE analysis are provided in Table 6. It can be observed that the fatigue and rutting strains obtained for the geosynthetic-reinforced pavement

Table 5. Input values for KENPAVE analysis

Layers	Thickness (mm)	Modulus (MPa)	Poisson's Ratio
Unreinforced asphalt concrete	216	2100	0.35
Polypropylene (PP) geogrid reinforced asphalt concrete (MIF = 1.45)	203	3045	0.35
Polyester (PET) geogrid reinforced asphalt concrete (MIF = 2.11)	178	4431	0.35
Glass geogrid composite (GGC) reinforced asphalt concrete (MIF = 2.77)	165	5817	0.35
Granular base & sub-base	483	200	0.35
Subgrade	-	75	0.40

Table 6. Output from KENPAVE analysis

Pavement sections	Asphalt layer thickness (mm)	Base & sub-base layer thickness (mm)	Fatigue strain (mm/mm)	Rutting strain (mm/mm)
Unreinforced pavement	216	483	1.69×10^{-4}	2.12×10^{-4}
Pavement with PP geogrid reinforced asphalt layer	203	483	1.469×10^{-4}	2.023×10^{-4}
Pavement with PET geogrid reinforced asphalt layer	178	483	1.361×10^{-4}	2.063×10^{-4}
Pavement with GGC reinforced asphalt layer	165	483	1.248×10^{-4}	2.051×10^{-4}

sections are consistently less than the limiting fatigue and rutting strains obtained for the unreinforced pavement sections for a design traffic of 20 MSA. This observation suggests that the inclusion of geosynthetic reinforcements in the asphalt layer leads to a reduction in asphalt layer thickness of about 12.5 mm (5.9%), 38 mm (17.6%), and 50 mm (23.5%), respectively, for the PP, PET, and GGC reinforcements considered in this study, without compromising the performance of pavement system.

Overall, the incorporation of geosynthetic reinforcements in asphalt layers has proven successful in extending fatigue life and a possible reduction in the thickness of asphalt layers. The extent of improvement depends on the bond characteristics, and tensile and mechanical properties of the geosynthetic reinforcement.

6. CONCLUSIONS

An experimental study on geosynthetic-reinforced asphalt layers was carried out using ABFT and DIC techniques to assess the influence of geosynthetic reinforcements on the fatigue performance of asphalt layers and corresponding mechanisms involved. The following conclusions can be drawn from the study:

The ABFT results demonstrated that all geosynthetic reinforcements considered in the study improved the fatigue performance of asphalt layers. Among them, and considering the products evaluated in this study, the performance of the glass geogrid composite was comparatively superior with an improvement factor of 38, followed by the polyester geogrid with an improvement factor of 27, and finally polypropylene geogrid with an improvement factor of 11, as a result of their working tensile and bonding properties.

The DIC technique was effective in investigating the mechanisms responsible for the enhancement of fatigue performance in asphalt layers. The presence of geosynthetic reinforcements delayed crack initiation by providing tensile reinforcement. A delay in crack initiation of 20 to 60 cycles was recorded in geosynthetic-reinforced specimens as compared to control specimens.

The DIC results indicate that tensile strains in all specimens were roughly 0.75% to 1% during the crack initiation phase. A maximum tensile strain of 11.2% was observed in control specimens at failure (345 cycles). The maximum tensile strain in geosynthetic-reinforced specimens was in the range of 2.7% to 3.8% at failure (4000 to 13 500 cycles), representing an overall reduction in tensile strain of 66% to 75% as compared to control specimens. This finding clearly demonstrates the enhanced fatigue performance attributable to the geosynthetic reinforcements.

The ABFT and DIC analysis indicate that all specimens failed at a vertical deformation of 12.8 mm to 13.7 mm. However, the number of cycles corresponding to failure showed considerable variance, and the presence of geosynthetic reinforcements improved resistance against load repetitions effectively by inducing reinforcement mechanisms. The DIC analysis also provided crucial data on crack growth characteristics.

Based on the test results, a design example has illustrated the reduction in thickness of asphalt layers when considering geosynthetic reinforcements. The reductions proposed were on the order of 5.9%, 17.6% and 23.5%, respectively, for the Polypropylene geogrid, Polyester geogrid and Glass geogrid composite reinforcements evaluated in this study.

Overall, it can be concluded that all geosynthetics adopted in the study were effective in enhancing the fatigue performance and hence, leading to a possible reduction in asphalt layer thickness. The glass geogrid composite used in this study showed a comparatively better response, followed by that of the polyester geogrid and finally the polypropylene geogrid.

NOTATION

Basic SI units are shown in parentheses.

a_1 & a_2	surface and base layer coefficients, respectively (dimensionless)
C	adjustment factor for variation in volumetric parameters of the asphalt mix (dimensionless)
CH	crack height (m)
COD	crack-opening displacement (m)
CW	crack width (m)
d_1 & d_2	thickness of surface and base layers, respectively (m)
I_{NF}	fatigue life improvement ratio (dimensionless)
l, b, and h	span length, width, and depth of ABFT specimen, respectively (m)
MIF	modulus improvement factor (dimensionless)
M_R	resilient Modulus of subgrade (Pa)
$M_{R\text{-}AC}$ & $M_{R\text{-}base}$	resilient modulus of asphalt and base layers, respectively (Pa)
MSA	million standard axles (dimensionless)
m_2	drainage coefficient of base layer (dimensionless)
N	number of load cycles (dimensionless)
NCM	normalized complex modulus (dimensionless)
N_f & N_R	fatigue and rutting lives of pavement system (dimensionless)
N_{GR}	fatigue life of geosynthetic-reinforced asphalt specimen (dimensionless)
N_i & N_0	ith and initial number of cycles, respectively (dimensionless)
N_{UR}	fatigue life of unreinforced asphalt specimen (dimensionless)
OBC	optimum binder content (dimensionless)
P	load (N)

P_0 & P_t initial and final serviceability indices, respectively (dimensionless)

S overall standard deviation (dimensionless)

S_i & S_0 stiffness at ith cycle and initial stiffness, respectively (Pa)

SN   structural number (dimensionless)

SN_{actual} & $SN_{reqd.}$ actual and required structural numbers, respectively (dimensionless)

V_a & V_b percentage air voids and percentage effective volume of bitumen in the asphalt mix used in bottom asphalt layer, respectively (dimensionless)

VD (V)   vertical deformation (m)

W_{18} total 18-kip traffic in equivalent single axle load (dimensionless)

Z_R standard normal variate (dimensionless)

ΔPSI   overall serviceability index (dimensionless)

δ vertical deformation (m)

ε maximum flexural (tensile) strain (dimensionless)

ε_t & ε_v limiting tensile (fatigue) and vertical compressive (rutting) strains for design fatigue and rutting lives, respectively (dimensionless)

σ_f maximum flexural stress (Pa)

ABBREVIATIONS

AASHTO   American Association of State Highway and Transportation Officials
ABFT   asphalt beam fatigue test
ASTM   American Society for Testing and Materials
CMD   cross-machine direction
CS   control specimen
DIC   digital image correlation
ESAL   equivalent single axle load
GGC   glass geogrid composite
MD   machine direction
MEPDG   mechanistic empirical pavement design guidelines
MORTH   Ministry of Road Transport and Highways
PET   polyester
PP   polypropylene

REFERENCES

AASHTO (1993). *Guide for Design of Pavement Structures*, American Association of State Highway and Transportation Officials, Washington, DC, USA.

Asphalt Institute (1981). MS-01: *Thickness Design – Asphalt Pavements for Highways and Streets*. Asphalt Institute, Lexington, KY, USA.

ASTM D4595 (2017). *Standard Test Method for Determining Tensile Properties of Geotextiles by the Wide-width Strip Method*. ASTM International, West Conshohocken, PA, USA.

ASTM D6927 (2015). *Standard Test Method for Marshall Stability and Flow of Asphalt Mixtures*. ASTM International, West Conshohocken, PA, USA.

ASTM D7460 (2010). *Standard Test Method for Determining Fatigue Failure of Compacted Asphalt Concrete Subjected to Repeated Flexural Bending*. ASTM International, West Conshohocken, PA, USA.

Caltabiano, M. A. (1990). *Reflection Cracking in Asphalt Overlays*. M.Phil., University of Nottingham, UK.

Chen, Q., Hanandeh, S., Abu-Farsakh, M. & Mohammad, L. (2018). Performance evaluation of full-scale geosynthetic reinforced flexible pavement. *Geosynthetics International*, **25**, No. 1, 26–36.

Choi, S. & Shah, S. P. (1997). Measurement of deformations on concrete subjected to compression using image correlation. *Experimental Mechanics*, **37**, 307–313.

Cleveland, G. S., Button, J. W. & Lytton, R. L. (2002). *Geosynthetic in Flexible and Rigid Pavement Overlay*, Report 1777-1. Texas Transportation Institute, Texas A&M University System, College Station, TX, USA.

Correia, N. S. & Zornberg, J. G. (2016). Mechanical response of flexible pavements enhanced with geogrid-reinforced asphalt overlays. *Geosynthetics International*, **23**, No. 3, 183–193.

Ferrotti, G., Canestrari, F., Pasquini, E. & Virgili, A. (2012). Experimental evaluation of the influence of surface coating on fiberglass geogrid performance in asphalt pavements. *Geotextiles and Geomembranes*, **34**, 11–18.

Gonzalez-Torre, I., Calzada-Peres, M. A., Vega-Zamanillo, A. & Castro-Fresno, D. (2015). Experimental study of the behavior of different geosynthetics as anti-reflective cracking systems using a combined-load fatigue test. *Geotextiles and Geomembranes*, **43**, No. 4, 345–350.

Grediac, M. (2004). The use of full-field measurement methods in composite material characterization: interest and limitations. *Composites Part A: Applied Science and Manufacturing*, **35**, No. 7–8, 751–761.

Gu, F., Luo, X., Luo, R., Lytton, R. L., Hajj, E. Y. & Siddharthan, R. V. (2016). Numerical modeling of geogrid-reinforced flexible pavement and corresponding validation using large-scale tank test. *Construction and Building Materials*, **122**, 214–230.

Hamrat, M., Boulekbache, B., Chemrouk, M. & Amziane, S. (2016). Flexural cracking behavior of normal strength, high strength and high strength fiber concrete beams, using digital image correlation technique. *Construction and Building Materials*, **106**, 678–692.

Imjai, T., Pilakoutas, K. & Guadagnini, M. (2019). Performance of geosynthetic-reinforced flexible pavements in full-scale field trials. *Geotextiles and Geomembranes*, **47**, No. 2, 217–229.

Kazimierowicz-Frankowska, K. (2020). Influence of geosynthetic reinforcement on maximum settlements of semi-rigid pavements. *Geosynthetics International*, **27**, No. 4, 348–363.

KENPAVE (2003). *A Computer Package for Pavement Analysis and Design*. University of Kentucky, Lexington, KY, USA.

Khodaii, A., Fallah, S. & Nejad, F. M. (2009). Effects of geosynthetics on reduction of reflection cracking in asphalt overlays. *Geotextiles and Geomembranes*, **27**, No. 1, 1–8.

Kim, Y. R. & Wen, H. (2002). Fracture energy from indirect tension test. *Journal of Association of Asphalt Paving Technologists*, **71**, 779–793.

Komatsu, T., Kikuta, H., Tuji, Y. & Muramatsu, E. (1998). Durability assessment of geogrid-reinforced asphalt concrete. *Geotextiles and Geomembranes*, **16**, No. 5, 257–271.

Kumar, V. V. & Saride, S. (2017). Use of digital image correlation for the evaluation of flexural fatigue behavior of asphalt beams with geosynthetic interlayers. *Transportation Research Record: The Journal of Transportation Research Board*, No. 2631, 55–64.

Kumar, V. V. & Saride, S. (2018). Evaluation of cracking resistance potential of geosynthetic-reinforced asphalt overlays using direct tensile strength tests. *Construction and Building Materials*, **162**, 37–47.

Mahal, M., Blanksvard, J., Taljsten, B. & Sas, G. (2015). Using digital image correlation to evaluate fatigue behavior of strengthened reinforced concrete beams. *Engineering Structures*, **105**, 277–288.

MORTH (2013). *Specifications for Road and Bridge Works*. Ministry of Road Transport and Highways, Government of India, New Delhi, India.

Pasquini, E., Bocci, M. & Canestrari, F. (2014). Laboratory characterization of optimised geocomposites for asphalt pavement reinforcement. *Geosynthetics International*, **21**, No. 1, 24–36.

Romeo, E. (2013). Two-dimensional digital image correlation for asphalt mixture characterization: interest and limitations. *Road Materials and Pavement Design*, **14**, No. 4, 747–763.

Safavizadeh, S. A., Wargo, A., Guddati, M. & Kim, Y. R. (2015). Investigating reflective cracking mechanisms in grid-reinforced asphalt specimens. *Transportation Research Record: The Journal of Transportation Research Board*, No. 2507, 29–38.

Sanders, P. J. (2001). *Reinforced Asphalt Overlays for Pavements*. PhD Thesis, University of Nottingham, UK.

Saride, S. & Kumar, V. V. (2017). Influence of geosynthetic-interlayers on the performance of asphalt overlays on pre-cracked pavements. *Geotextiles and Geomembranes*, **45**, No. 3, 184–196.

Saride, S. & Kumar, V. V. (2019a). Estimation of service life of geosynthetic-reinforced asphalt overlays from beam and large-scale fatigue tests. *Journal of Testing and Evaluation*, **47**, No. 4, 2693–2716.

Saride, S. & Kumar, V. V. (2019b). Reflection crack assessment using digital image analysis. In: *Frontiers in Geotechnical Engineering, Developments in Geotechnical Engineering* (ed. G. M. Latha). Springer, Singapore, pp. 139–156, https://doi.org/10.1007/978-981-13-5871-5_8.

Sudarsanan, N., Karpurapu, R. & Amrithalingam, V. (2018). An investigation on the interface bond strength of geosynthetic-reinforced asphalt concrete using Leutner shear test. *Construction and Building Materials*, **186**, 423–437.

Sudarsanan, N., Arulrajah, A., Karpurapu, R. & Amrithalingam, V. (2019). Digital image correlation technique for measurement of crack propagation in reinforced asphalt concrete beams under fatigue loading. *Journal of Materials in Civil Engineering*, **31**, No. 8, https://doi.org/10.1061/(ASCE)MT.1943-5533.0002743.

Sudarsanan, N., Arulrajah, A., Karpurapu, R. & Amrithalingam, V. (2020). Fatigue performance of geosynthetic reinforced asphalt concrete beams. *Journal of Materials in Civil Engineering*, **32**, No. 8, https://doi-org./10.1061/(ASCE)MT.1943-5533.0003267.

Virgili, A., Canestrari, F., Grilli, A. & Santagata, F. A. (2009). Repeated load test on bituminous systems reinforced by geosynthetics. *Geotextiles and Geomembranes*, **27**, No. 3, 187–195.

Wargo, A., Safavizadeh, S. A. & Kim, Y. R. (2017). Comparing the performance of fiberglass grid with composite interlayer systems in asphalt concrete. *Transportation Research Record: The Journal of Transportation Research Board*, No. 2631, 123–132.

Zamora-Barraza, D., Calzada-Peres, M. A., Castro-Fresno, D. & Vega-Zamanillo, A. (2011). Evaluation of anti-reflective cracking systems using geosynthetics in the interlayer zone. *Geotextiles and Geomembranes*, **29**, No. 2, 130–136.

Zofka, A. & Maliszewski, M. (2019). Practical overlay design for geogrid reinforcement of asphalt layers. *Road Materials and Pavement Design*, **20**, No. sup1, S163–S182.

Zornberg, J. G. (2017a). Functions and applications of geosynthetics in roadways: part 1. *Geosynthetics*, 34–40.

Zornberg, J. G. (2017b). Functions and applications of geosynthetics in roadways: part 2. *Geosynthetics*, 34–40.

The Editor welcomes discussion on all papers published in Geosynthetics International. Please email your contribution to discussion@geosynthetics-international.com by 15 June 2022.